Frontiers of Information Technology & Electronic Engineering
www.jzus.zju.edu.cn; engineering.cae.cn; www.springerlink.com
ISSN 2095-9184 (print); ISSN 2095-9230 (online)
E-mail: jzus@zju.edu.cn

Infrared Earth sensor with a large field of view for low-Earth-orbiting micro-satellites*

Hao WANG†‡[1], Zhi-yuan WANG[1], Ben-dong WANG[1], Zhong-he JIN[1], John L. CRASSIDIS[2]

[1]*School of Aeronautics and Astronautics, Zhejiang University, Hangzhou 310027, China*

[2]*Department of Mechanical and Aerospace Engineering, University at Buffalo, the State University of New York, Buffalo 14260-4400, USA*

†E-mail: roger@zju.edu.cn

Received July 18, 2019; Revision accepted Dec. 24, 2019; Crosschecked May 18, 2020; Published online July 20, 2020

Abstract: Infrared Earth sensors are widely used in attitude-determination and control systems of satellites. The main deficiency of static infrared Earth sensors is the requirement of a small field of view (FOV). A typical FOV for a static infrared Earth sensor is about 20° to 30°, which may not be sufficient for low-Earth-orbiting micro-satellites. A novel compact infrared Earth sensor with an FOV of nearly 180° is developed here. The Earth sensor comprises a panoramic annular lens (PAL) and an off-the-shelf camera with an uncooled complementary-metal-oxide-semiconductor (CMOS) infrared sensor. PAL is used to augment FOV so as to obtain a complete infrared image of the Earth from low-Earth-orbit. An algorithm is developed to compensate for the distortion caused by PAL and to calculate the vector of the Earth. The new infrared Earth sensor is compact with low power consumption and high precision. Simulated images and on-orbit infrared images obtained via the micro-satellite ZDPS-2 are used to assess the performance of the new infrared Earth sensor. Experiments show that the accuracy of the Earth sensor is about 0.032°.

Key words: Infrared Earth sensor; Micro-satellite; Attitude determination system
https://doi.org/10.1631/FITEE.1900358 **CLC number:** V447

1 Introduction

Earth-horizon sensors are widely used in mid- to high-Earth-orbiting satellites, which fly over the Earth at heights above 2000 km (Gontin and Ward, 1987; Deng et al., 2013). They are important components of the attitude determination and control system of satellites. Infrared horizon sensors are also called infrared Earth sensors, and are used to provide vectors with respect to the Earth. Traditionally, an infrared Earth sensor operates on the principle of detecting the infrared emission of the upper Earth atmosphere, composed of mainly carbon dioxide and providing a stable signal (Hoffman, 1976). Earth-horizon sensors detect the angle of the Earth horizon with respect to the sensor's axis when the horizon is within the sensor's field of view (FOV). Generally, there are two kinds of infrared Earth sensors used to measure the Earth's horizon or outer edge (Markley and Crassidis, 2014). One is the dynamic Earth sensor, and the other is the static Earth sensor. The infrared detector of a dynamic Earth sensor rotates along a certain axis to detect the horizon, and emits two pulses if the horizon is detected. The time interval between the two pulses is measured and compared with a standard time interval to calculate the angle. In other words, the dynamic Earth sensor scans the Earth. The static Earth sensor, on the other hand, has no movable parts. It operates

‡ Corresponding author

* Project supported by the National Science Fund for Distinguished Young Scholars, China (No. 6152403)

ORCID: Hao WANG, https://orcid.org/0000-0002-0383-7258

on the principle of taking an infrared image of the Earth's horizon and then finding the center of the Earth in its focal plane. The Earth's center and the center of the sensor (which is always the same as the center of the focal plane) are used to calculate the Nadir angle for attitude determination (Alperovich and Topaz, 1995; Soto-Romero et al., 2001).

Dynamic Earth sensors are often larger, heavier, and consume much more power than static Earth sensors because of their movable components. Vibration caused by these components and infrared disturbances caused by clouds or atmosphere are two factors to be considered for a precise detection. Static Earth sensors, however, have a relatively small FOV (usually less than 60°) (Falbel, 2004). The micro-satellite industry has boomed in recent years (Swartwout, 2013), but dynamic infrared Earth sensors are not well suited for these satellites because of their size and power consumption. Compact and low-power-consumption sensors are generally required in micro-satellite applications. On the micro-sized microwave atmospheric satellite (MicroMAS) (Nguyen et al., 2018), compact infrared Earth sensors were applied and evaluated (MAI-SES, 2016). Micro-satellites are used mostly in low-Earth orbit (LEO). This means static Earth sensors with a large FOV are needed. Assuming a perfectly spherical Earth, the FOV can be calculated using simple geometric reasoning as

$$\mathrm{FOV} = 2\arctan\left(\frac{r_\mathrm{e}}{r_\mathrm{e}+r_\mathrm{h}}\right), \tag{1}$$

where r_e is the radius of the Earth and r_h is the height of the orbit. For example, as shown in Fig. 1, FOV should be at least 120° to obtain the Earth's infrared image when a static Earth sensor is used in a 500 km LEO.

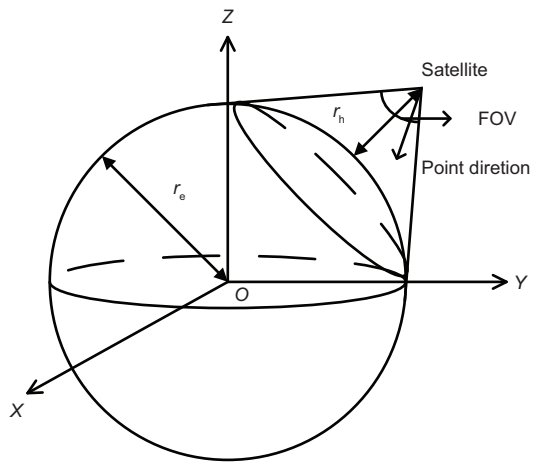

Fig. 1 View of the Earth from a satellite

To meet the requirements of micro-satellites, a novel infrared Earth sensor composed of a panoramic annular lens (PAL) and a complementary-metal-oxide-semiconductor (CMOS) infrared camera is designed. PAL is used to make FOV large enough to fully view and measure the Earth in LEO. A compensation algorithm is developed for PAL distortions of the images from the Earth sensor. The CMOS infrared camera used is a commercial off-the-shelf product. After obtaining an image of the Earth, the detection of Earth's horizon is a matter of image processing. The main principle is to find the center of the Earth in the infrared Earth image, and then to calculate the Earth vector. There are many mature image-processing algorithms that can be used. It is convenient to choose a computationally efficient algorithm.

The infrared Earth sensor developed here has the features of being compact with low power consumption and high precision. Ground-simulated images and on-orbit infrared images of the Earth are used to assess the performance of the new infrared Earth sensor. These on-orbit images were obtained by a micro-satellite called ZDPS-2, on which a prototype of the infrared Earth sensor was equipped. The specifications of ZDPS-2 and the infrared Earth sensor are shown in Table 1.

Table 1 Specifications of the infrared Earth sensor and ZDPS-2

Specification	Infrared Earth sensor	ZDPS-2
Weight (kg)	0.2	20
Dimension (mm×mm×mm)	40×40×55	250×250×250
Power supply (W)	1.4	13
Refreshing frequency (Hz)	3	–

2 Configuration of the infrared Earth sensor

2.1 Hardware

The infrared Earth sensor is composed of an infrared camera, PAL, and image-processing circuits. The lens follows the principle of the flat-cylinder perspective (Niu et al., 2007). Unlike a traditional optical system, such as the central-convergence perspective, the PAL system projects the cylindrically

panoramic view of 360° around the optical axis to an annular area on a plane. There are two parts in the two-dimensional (2D) image plane via PAL, image area and blind area (Fig. 2), where Z represents the optical axis and α_s and β_s denote the angles of the imaging and blind areas, respectively. Each of the concentric circles on the image plane corresponds to the gathering of points with the same angle around the cylinder in the object space. The value of β_s is about 30°, meaning that the Earth could not be detected if it falls into the blind area. The Earth's radius is about 6378 km, so the sensor would fail to detect the Earth for an orbital altitude above 6378 km. Thus, this infrared Earth sensor is suitable for satellites with an orbit lower than 6378 km. The Earth sensor detects infrared light emitted from the Earth with a CMOS infrared camera, while other wavelengths are filtered. A filter is added to the surface of the lens to allow only specific wavelengths to pass. Some important specifications of the infrared camera are listed in Table 2.

2.2 Image-processing algorithm

Once the Earth's image is obtained, the center of the Earth is calculated via image processing. This processing consists of a series of procedures. First, the Earth's image is converted to a binary image. Next, edge information is extracted from the binary image. Then, the geometric centers of the Earth in these gray-scale images are found based on the edge information. Finally, the center is used to calculate the Earth vector. As edge extraction and detection play an important role in image processing, it is important to choose an effective algorithm. Many mature algorithms have been used for edge detection, such as the Sobel, Roberts cross, and Canny operators (Sharifi et al., 2002). Among these, the Sobel operator is a classical algorithm with many advantages such as high computational efficiency and good processing results for simple graphics. Thus, it is a suitable on-orbit image processing algorithm for the infrared Earth sensor. The Sobel operator performs a 2D-spatial-gradient measurement on images when detecting an edge. The principle involves estimating the gradient of a digitized picture at a point via vector summation of the four possible central-gradient estimates in a 3×3-pixel neighborhood. For a 3×3 neighborhood, each simple central-gradient estimate is a vector sum of a pair of orthogonal vectors. Each orthogonal vector is a directional derivative estimate multiplied by a unit vector specifying the derivative's direction. The vector sum of these four simple gradient estimates amounts to a vector sum of the eight directional-derivative vectors. Thus, for a point on a Cartesian grid with eight neighbors, the density values p are provided as shown in Fig. 3. The magnitude of the directional-derivative-estimation vector $\boldsymbol{g}$ for a given neighbor is defined as

$$\|\boldsymbol{g}\| = \frac{\text{density difference}}{(\text{distance to the neighbor})^2}. \tag{2}$$

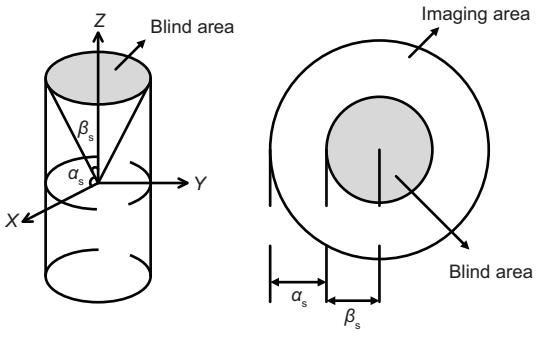

Fig. 2 Image plane of the panoramic annular lens

Table 2 Specifications of the infrared camera

Component	Specification
Sensor	CCD/CMOS
Pixel	25 μs
Focal length	2.3 mm
Aperture value	2.0
Dimension	Φ40 mm×30 mm
Frequency	8–14 μm
FOV	180° × 360°
Iris	Fixed
Mount	C-mount
Weight	40 g

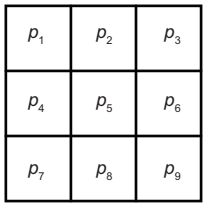

Fig. 3 A 3×3-pixel neighborhood

There are four antipodal pairs: (p_1, p_9), (p_3, p_7), (p_2, p_8), and (p_4, p_6). Then distances are defined according to the numbers of pixels between these pairs. The distance to the neighbor in the first

two pairs is defined as four, while that in the other two pairs is defined as two. As a result, $\boldsymbol{g}$ is given by

$$\boldsymbol{g}=\left(\frac{p_1-p_9}{4}\boldsymbol{i}+\frac{p_2-p_8}{2}\boldsymbol{j}+\frac{p_3-p_7}{4}\boldsymbol{k}+\frac{p_4-p_6}{2}\boldsymbol{\ell}\right), \tag{3}$$

where $\boldsymbol{i}$, $\boldsymbol{j}$, $\boldsymbol{k}$, and $\boldsymbol{\ell}$ denote four directions. Here, $\boldsymbol{i}$ is a vector pointing from p_1 to p_9, and $\boldsymbol{k}$ is another vector pointing from p_3 to p_7. They are orthogonal to each other. Vector $\boldsymbol{j}$ is in the vertical direction, while vector $\boldsymbol{\ell}$ is in the horizonal direction. They are orthogonal to each other as well.

Then, the gradient summation $\boldsymbol{G}$ is defined as

$$\boldsymbol{G}\equiv\begin{bmatrix}\dfrac{p_1+p_3-p_7-p_9}{4}+\dfrac{p_2-p_8}{2}\\ \dfrac{p_1+p_3-p_7-p_9}{4}+\dfrac{p_4-p_6}{2}\end{bmatrix}. \tag{4}$$

To simplify calculations, $\boldsymbol{G}$ is scaled by four. Thus, the magnitude of the vector summation is

$$\begin{aligned}\left\|\boldsymbol{G}'\right\|\equiv&\|4\boldsymbol{G}\|\\ =&(p_1+p_3-p_7-p_9+2p_2-2p_8)^2\\ &+(p_1+p_3-p_7-p_9+2p_4-2p_6)^2.\end{aligned} \tag{5}$$

A pixel at location p_5 is defined as an edge pixel if $\left\|\boldsymbol{G}'\right\|\geq T$, where T is a specified threshold. The key point to the Sobel algorithm is to set an appropriate threshold. Considering the instability of the working environment in orbit, it is difficult to determine an accurate threshold on the ground. Thus, the threshold is set by trial and error to four times the mean value of the image being processed. This is a conservative value to ensure the continuity of the edge.

On the other hand, this value may lead to an increase in the interference points and thick edges, which would affect the speed of the image-processing algorithm. To simplify the following calculation, an algorithm of erosion is applied (Gonzalez et al., 2013). The algorithm of image erosion is a type of image-morphological processing with many advantages including high processing speed and ease of implementation. A structure element is used to complete the erosion algorithm, given by

$$\begin{bmatrix}0&1&0\\1&1&1\\0&1&0\end{bmatrix}, \tag{6}$$

where 1 and 0 are the pixels' values. According to the structure element, only if all four pixels adjacent to a pixel are valued 1, will the pixel's value be kept as "1;" otherwise, it will be set to "0." The edge-detection algorithm is tested via a prototype of the Earth sensor. The results are shown in Fig. 4. Here, Fig. 4a is the raw image, Fig. 4b shows the edge detected after the Sobel operation, and Fig. 4c shows the edge after erosion processing. As can be seen, the erosion process produces a sharper edge, with fewer points and less disturbance in the image. Thus, the quality of the image's edge is improved, and computational complexity will be reduced in postprocessing. Once the edge is detected, the next step is to obtain its geometric center.

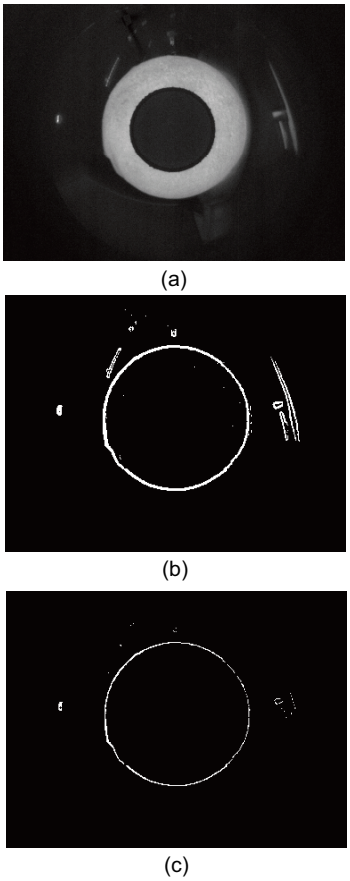

Fig. 4 Image processing: (a) raw image; (b) edge detected; (c) edge detected after erosion

2.3 Geometric-center-determination method

As previously mentioned, PAL projects the cylindrically panoramic view of 360°. Its imaging formula is given by

$$D=f\cdot\theta, \tag{7}$$

where f is the focal length of PAL, θ is the angle between the incident light and the lens' normal, and D is the distance between the lens' center and the image of the incident light upon the image plane. All edge points on the image plane are mapped one to one onto the unit image-sphere to reduce the distortion caused by the lens. According to the lens-imaging formula, the coordinates of one point can be derived from its image's coordinates:

$$\begin{cases} x_1 = R\sin\theta\dfrac{x}{\sqrt{x^2+y^2}}, \\ y_1 = R\sin\theta\dfrac{y}{\sqrt{x^2+y^2}}, \\ z_1 = R\cos\theta, \end{cases} \tag{8}$$

where x_1, y_1, and z_1 are the point's coordinates, while x and y are the coordinates of its image in the image plane. The angle θ is determined from Eq. (7) and R is the radius of the unit image-sphere, which is normally set to 1.

Substituting the edge dots obtained from Fig. 4c into Eq. (8), there will be a new image on the image sphere, as shown in Fig. 5.

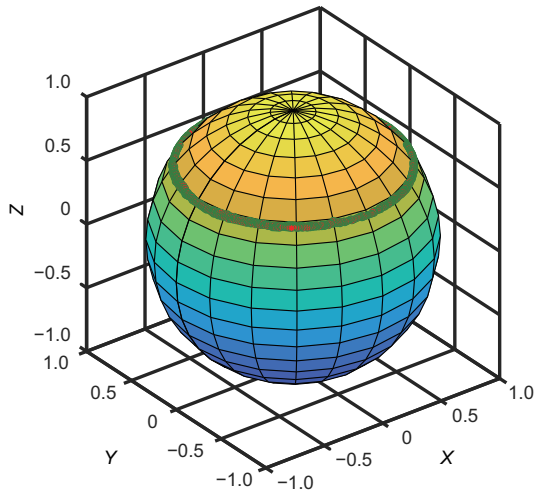

Fig. 5 Earth contour

The edge points form a circle in the image sphere, called "circle E" hereafter. The circle's radius can be estimated as a function of the orbital altitude. There are incorrect disturbance points on the image sphere. Some are junction points of the blind and image areas, while others are caused by disturbing light or heat. The former can be easily removed because they are fixed interferences of PAL with constant coordinates. The remaining disturbance points are screened out via a screening algorithm. The points left are then used to determine circle E with curve-fitting algorithms. There are two widely used techniques in curve fitting, clustering (such as the Hough transformation) and least-squares fitting. These two algorithms have advantages and disadvantages (Leavers, 1993; Torii and Imiya, 2007); for example, the Hough transformation is good at finding an optimal solution in the whole parameter space, and it is robust to disturbance points. The main issue with the Hough transformation is that its precision is related to the step of the parameter space; an accurately predicted circle radius is needed to obtain a high-precision result. In contrast, the least-squares-fitting approach has lower computational cost and requires no prior information concerning the radius of the image circle, but it is easily affected by the disturbance points. Considering the requirements of accuracy and limited computing time, both methods are used. In the initial measurement, i.e., for the first frame of an image stream provided by the Earth sensor, the Hough transformation is used to calculate the vector of the Earth's center. From the second image on, the least-squares method is used to calculate this vector.

2.3.1 Hough transformation

Setting $O_{\mathrm{E0}}(x_0, y_0, z_0)$ as the coordinates of the center of circle E, the function of the plane is given by

$$x_0(x-x_0)+y_0(y-y_0)+z_0(z-z_0)=0. \tag{9}$$

Note that x, y, and z are edge-point coordinates in the camera's coordinate system, which is identical to the satellite's body-coordinate system. This plane equation can be rewritten as

$$x_0x+y_0y+z_0z=r_l^2, \tag{10}$$

where r_l refers to the distance between the center of circle E and the center of the image sphere, which would be known in advance. Transferring Eq. (10) from rectangular coordinates to spherical coordinates yields

$$\begin{cases} x_0 = r_l\sin\beta\cos\alpha, \\ y_0 = r_l\sin\beta\sin\alpha, \\ z_0 = r_l\cos\beta, \end{cases} \tag{11}$$

where α is the azimuthal angle from the center of circle E and β is the polar angle from the center of

circle E. Substituting Eq. (11) into Eq. (10), the plane function is (Torii and Imiya, 2007)

$$x\sin\beta\cos\alpha + y\sin\beta\sin\alpha + \cos\beta = r_l. \tag{12}$$

The value of r_l calculated in the current image is set as the initial value of the next image. Assuming negligible attitudinal motion over the course of taking multiple images, the vectors of the Earth's center will not significantly change between two images. Then, x_0, y_0, and z_0 are calculated using the Hough transformation. A screening test is given by

$$\begin{aligned}(1-k)r &\le \sqrt{(x-x_0)^2+(y-y_0)^2+(z-z_0)^2}\\ &\le (1+k)r,\end{aligned} \tag{13}$$

where r is the theoretical distance from the edge to the center of circle E (coordinates $O_{E0}(x_0, y_0, z_0)$), and k is the coefficient of the confidence interval. The value of k is set to 0.05 in the actual calculation. The points that do not match inequality (13) are considered to be disturbance points. This is the screening algorithm mentioned above. x, y, and z are all measurements, so they do contain noise. Also, x_0, y_0, and z_0 are calculated using the Hough transformation, and contain noise as well. Finally, r_l has noise too, but much less than the aforementioned noisy terms, with little influence upon the overall performance.

2.3.2 Least-squares estimation

For the infrared Earth sensor, the equation of circle E (O_{E0}) is expressed by Eq. (10). In this equation, r_l refers to the distance between the center of circle E and the center of the image sphere, which is constant when the orbital altitude of the satellite is stationary (Chen and Chung, 2001). Eq. (12) can be rewritten as

$$\frac{\sin\beta\cos\alpha}{\cos\beta}x + \frac{\sin\beta\sin\alpha}{\cos\beta}y + z = \frac{r_l}{\cos\beta}. \tag{14}$$

Then, the following expression is obtained:

$$z = -\frac{\sin\beta\cos\alpha}{\cos\beta}x - \frac{\sin\beta\sin\alpha}{\cos\beta}y + \frac{r_l}{\cos\beta}. \tag{15}$$

To simplify the equation, we define

$$\begin{aligned}[a_1\ a_2\ a_3] &= \left[-\frac{\sin\beta\cos\alpha}{\cos\beta}\ -\frac{\sin\beta\sin\alpha}{\cos\beta}\ \frac{r_l}{\cos\beta}\right]\\ &= \left[-\frac{x_0}{z_0}\ -\frac{y_0}{z_0}\ \frac{r_l^2}{z_0}\right].\end{aligned} \tag{16}$$

A least-squares model based on Eq. (15) can be built as

$$z_i = a_1x_i + a_2y_i + a_3, \tag{17}$$

or

$$\boldsymbol{z} = \boldsymbol{H\theta}, \tag{18}$$

where $\boldsymbol{H}$ is the design matrix and $\boldsymbol{\theta}$ is the parameter vector to be determined:

$$\boldsymbol{H} = \begin{bmatrix} x_1 & y_1 & 1\\ x_2 & y_2 & 1\\ \vdots & \vdots & \vdots\\ x_n & y_n & 1\end{bmatrix}, \boldsymbol{\theta} = \begin{bmatrix} a_1 & a_2 & a_3\end{bmatrix}^{\mathrm{T}}. \tag{19}$$

The least-squares estimate is given by

$$\hat{\boldsymbol{\theta}} = \left(\boldsymbol{H}^{\mathrm{T}}\boldsymbol{H}\right)^{-1}\boldsymbol{H}^{\mathrm{T}}\boldsymbol{z}. \tag{20}$$

Note that $\boldsymbol{H}$ contains noise, so the total least-squares method should be employed (Crassidis and Markley, 2016). However, as the signal-to-noise ratio is sufficiently large, the standard least-squares method can provide an acceptable accuracy.

2.3.3 Algorithm for the Earth sensor

The block diagram of the Earth sensor's algorithm is shown in Fig. 6. Because the orbital altitude of the satellite will slightly change with its operation, r_l will accordingly change. It is necessary to make r_l adaptive because if r_l is set to a fixed value, an error will inevitably occur. As mentioned previously, the result of the Hough transformation is sensitive to r_l, while the least-squares algorithm has no requirement for this, and the value of r_l is included in the calculation result. Therefore, the iterative algorithm of the Hough transformation and the least-squares algorithm are both used in this design to calculate the center of the Earth via the following steps:

1. Input a possible r_{l0} to the Hough transformation, and then obtain a direction vector to the Earth's center O_{E0}.
2. Noisy points are discarded and the least-squares algorithm is applied to the remaining points to obtain the new values of O_E and r_l (O_{E1} and r_{l1}).
3. Comparing r_{l0} and r_{l1}, if the difference is more than a threshold (set to 0.001 for this design), return to step 1 and apply Hough transformation till r_{lk} converges.
4. End the loop.

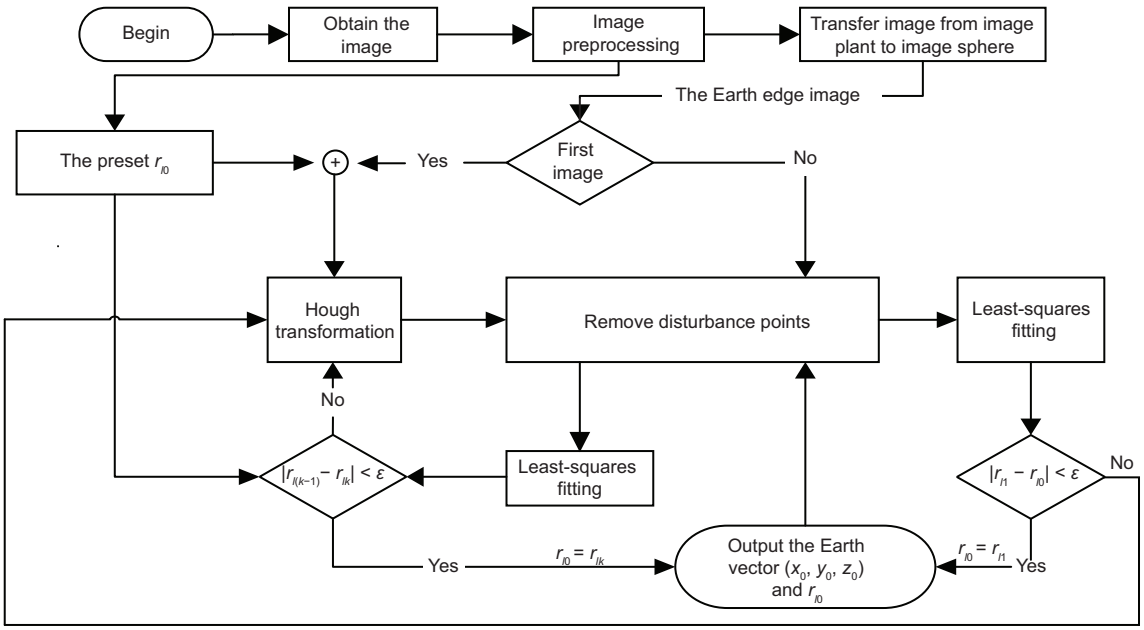

Fig. 6 Block diagram of the Earth sensor's algorithm

The outputs O_{E0} and r_{l0} from the previous images are used as a condition in the following operation, because the value of r_l slowly changes in space. If the difference between r_{l1} and r_{l0} is less than an infinitesimal amount, O_{E1} and r_{l1} will be used in the next frame. Otherwise, input r_{l1} to the Hough transformation and repeat the previous iterative algorithm until convergence. This procedure can ensure the operational accuracy and improve the computing efficiency (if the altitude of the orbit is nearly constant, image processing will be as simple as applying a least-squares algorithm once from the second frame onwards).

3 Experiments and analysis

3.1 Calibration of PAL

The PAL lens must be calibrated before constructing the simulated system. The PAL lens' projection model is given by

$$r(\theta) = k_1\theta + k_2\theta^3 + \ldots, \tag{21}$$

where k_1 and k_2 are first calibrated. Higher-order terms can be incorporated if needed. The PAL lens' real projection origin is also considered. A two-axis rotary table and an infrared source are used in calibrating these parameters. The detailed procedures can be found in Zhang et al. (2009).

3.2 Ground-simulation system

A ground-simulation system was developed to assess the measurement performance of the Earth sensor. This system was composed of several parts:

1. A single-axis high-precision rotary table with a control accuracy of 0.005°.

2. A simulated infrared Earth, which was a hollow metal ball filled with hot water. During the test, a temperature-control system was used to keep the ball at a preset temperature.

3. A heat-insulation base, which was used to reduce the heat conduction from the device.

4. A computer, which was used to control the rotation of the table and also to receive data from the Earth sensor.

The physical diagram of the system is shown in Fig. 7a, and a schematic is shown in Fig. 7b.

The diameter of the simulated infrared Earth was 38 cm, so the distance between the lens and the infrared Earth-sensor simulator was set to 3 cm. At this distance, the simulated Earth was of the same size as the actual Earth seen by a satellite at an altitude of 1000 km. As shown in Fig. 8, α_{r} is the rotary table's rotation angle and α_{n} is the Nadir angle. Also, $\boldsymbol{V}_{\mathrm{e}}$ is the Earth vector to be detected. The value for α_{n} can be calculated from $\boldsymbol{V}_{\mathrm{e}}$, because the vector $\boldsymbol{O}_{\mathrm{c},z}$ is known as [0 0 1]. α_{r} was set from $-10.25°$ to $9.65°$ at an interval of $0.1°$. Also, $\boldsymbol{V}_{\mathrm{e}}$ was

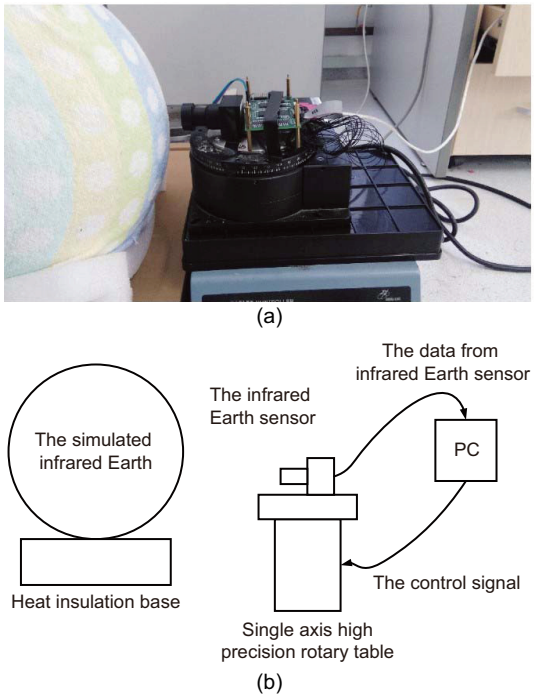

Fig. 7 Testing system: (a) test setup; (b) schematic

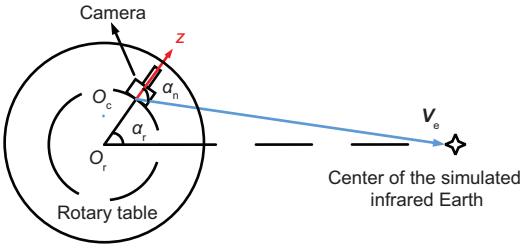

Fig. 8 Schematic of the simulation

detected 100 times at each α_r to make statistically rigorous detections. Then, α_n was calculated 100 times accordingly. For example, as shown in Fig. 9, α_n was calculated 100 times with three different α_r's at 1.85°, 3.85°, and 5.85°, respectively. According to the chi-squared test, the measurements were normally distributed.

After that, the residual error of α_n was calculated for each α_r. As shown in Fig. 10, there were 16 200 measurements with α_r ranging from −10.25° to 9.65° at an interval of 0.1°. According to the chi-squared test, the residual errors were normally distributed with a −0.0005° mean. The standard deviation and root mean square were both 0.032°.

4 Data validation

The Earth sensor was carried on the ZDPS-2 satellite, which was developed by Zhejiang

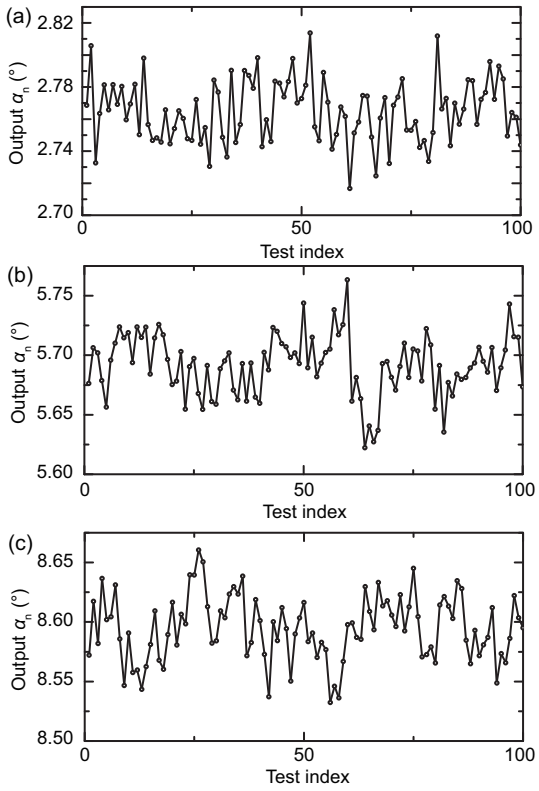

Fig. 9 Measurements at three different inputs with three different α_r's: (a) 1.85°; (b) 3.85°; (c) 5.85°

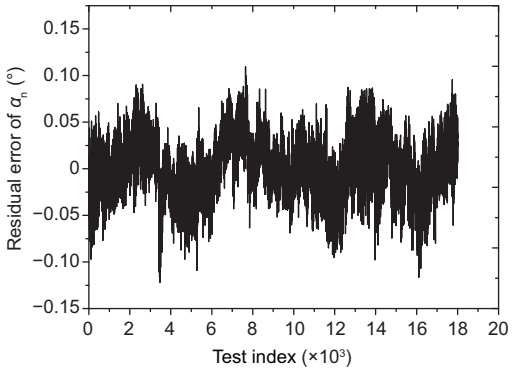

Fig. 10 Residual error of the Nadir angle

University and launched in September 2015. Several infrared images of the Earth were taken in orbit, and two of them were selected for analysis and processing based on the previous algorithm. Fig. 11a was obtained when the satellite was three-axis stabilized. The satellite was pointing at the Earth at that time, so the true angle of the Earth should be zero for an ideal attitude-control system. The image-processing result for the calculated angle between the Earth and the satellite was 3.26°. Fig. 12a was obtained when the satellite was in Sun-pointing mode, and the angle of the Earth was determined to be 102°, while

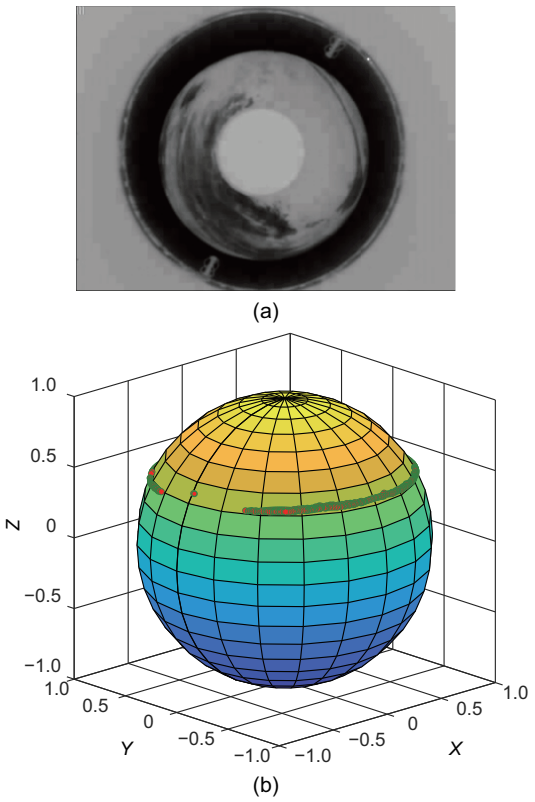

Fig. 11 Three-axis-stabilized mode: (a) raw image; (b) circle *E* without noisy points

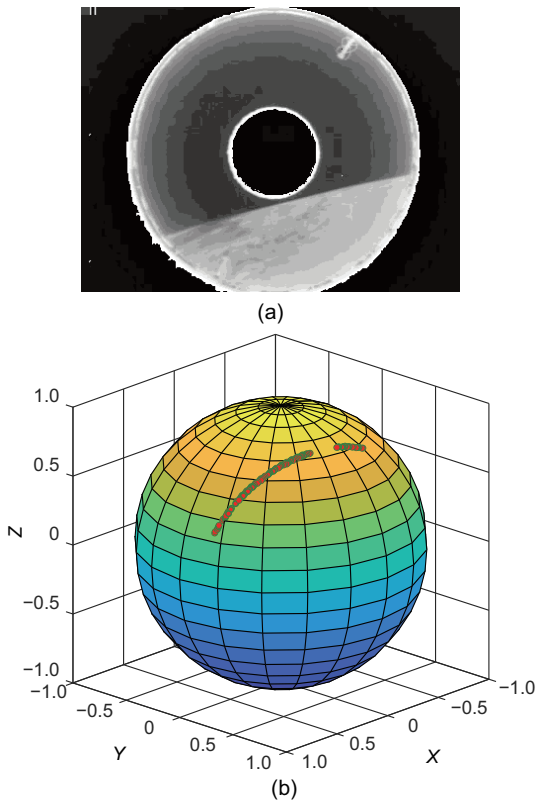

Fig. 12 Sun-pointing mode: (a) raw image; (b) circle *E* without noisy points

the result of image processing was 100.28°, showing good agreement. It was difficult to perform a more accurate evaluation because the satellite's attitude-control precision was about 5°. However, the results obtained were consistent with the expected values.

5 Conclusions

A new Earth sensor has been developed. The measurement accuracy of the sensor and its algorithm were proven via ground-based simulations. Through extensive tests and analyses, the following conclusions could be drawn. The Earth sensor which has a large field of view with a fixed panoramic lens is suitable for medium- and low-Earth-orbiting satellites. The new design avoids standard issues with other Earth sensors in these orbits. It also has the advantages of small size, light weight, and low power consumption. The sensor can maintain relatively high precision at large angles of inclination to the Earth. The ground tests showed that the measurement accuracy can be guaranteed within 1° when the inclination of the sensor is about 50° to the Earth. The system has high stability and precision for Nadir-pointing scenarios (the inclined angle is less than 10°) with a standard-deviation error below 0.032°.

Contributors

Hao WANG designed the research. Zhi-yuan WANG and Ben-dong WANG acquired and processed the data. Hao WANG drafted the manuscript. Zhong-he JIN and John L. CRASSIDIS helped organize the manuscript. Hao WANG, Zhi-yuan WANG, and Ben-dong WANG revised and finalized the paper.

Compliance with ethics guidelines

Hao WANG, Zhi-yuan WANG, Ben-dong WANG, Zhong-he JIN, and John L. CRASSIDIS declare that they have no conflict of interest.

References

Alperovich V, Topaz JM, 1995. Correction of errors due to profile shape in static Earth horizon sensors. Proc 9th Meeting on Optical Engineering in Israel, p.336-344. https://doi.org/10.1117/12.211207

Chen TC, Chung KL, 2001. An efficient randomized algorithm for detecting circles. *Comput Vis Image Underst*, 83(2):172-191. https://doi.org/10.1006/cviu.2001.0923

Crassidis JL, Markley FL, 2016. Three-axis attitude estimation using rate-integrating gyroscopes. *J Guid Contr Dynam*, 39(7):1513-1526.

Deng LL, Mei ZW, Tu ZJ, et al., 2013. A carbon dioxide radiance model of the Earth planet using the conical Earth sensor data. Proc SPIE Remote Sensing, Article 888 91U. https://doi.org/10.1117/12.2029065

Falbel G, 2004. A low weight/power/cost infrared Earth sensor. Proc IEEE Aerospace Conf, p.2716-2722. https://doi.org/10.1109/AERO.2004.1368068

Gontin R, Ward K, 1987. Horizon sensor accuracy improvement using Earth horizon profile phenomenology. Proc Guidance, Navigation and Control Conf, p.1495-1502. https://doi.org/10.2514/6.1987-2598

Gonzalez RC, Woods RE, Eddins SL, 2013. Digital Image Processing Using MATLAB. Prentice-Hall, Inc., Upper Saddle River, USA.

Hoffman JW, 1976. Stability of the infrared Earth horizon at 15 microns. *J Spacecr Rock*, 13(10):626-628. https://doi.org/10.2514/3.27936

Leavers VF, 1993. Which Hough transform? *CVGIP Image Underst*, 58(2):250-264. https://doi.org/10.1006/ciun.1993.1041

MAI-SES, 2016. Static Earth Sensor Product Specification. Maryland Aerospace Inc., Crofton, USA. https://www.cubesatshop.com/wp-content/uploads/2016/06/MAI-SES-Specifications-20150827.pdf [Accessed on July 20, 2019].

Markley FL, Crassidis JL, 2014. Fundamentals of Spacecraft Attitude Determination and Control. Springer, New York, USA.

Nguyen T, Cahoy K, Marinan A, 2018. Attitude determination for small satellites with infrared Earth horizon sensors. *J Spacecr Rock*, 55(6):1466-1475. https://doi.org/10.2514/1.A34010

Niu S, Bai J, Hou XY, et al., 2007. Design of a panoramic annular lens with a long focal length. *Appl Opt*, 46(32):7850-7857. https://doi.org/10.1364/AO.46.007850

Sharifi M, Fathy M, Mahmoudi MT, 2002. A classified and comparative study of edge detection algorithms. Proc Int Conf on Information Technology: Coding and Computing, p.117-120. https://doi.org/10.1109/ITCC.2002.1000371

Soto-Romero G, Bony F, Simonne JJ, et al., 2001. Micro infrared Earth sensor project: an integrated IR camera for Earth remote sensing. Int Symp on Remote Sensing, p.176-187. https://doi.org/10.1117/12.450659

Swartwout M, 2013. The first one hundred CubeSats: a statistical look. *J Small Satell*, 2(2):213-233.

Torii A, Imiya A, 2007. The randomized-Hough-transform-based method for great-circle detection on sphere. *Patt Recogn Lett*, 28(10):1186-1192. https://doi.org/10.1016/j.patrec.2007.02.002

Zhang GJ, Wei XG, Fan QY, et al., 2009 Method and Device for Calibration of Digital Celestial Sensor. US Patent 7 822 572.